Article

Effective Photocatalytic Activity of Mixed Ni/Fe-Base Metal-Organic Framework under a Compact Fluorescent Daylight Lamp

Vinh Huu Nguyen [1], Trinh Duy Nguyen [1,*], Long Giang Bach [1], Thai Hoang [2], Quynh Thi Phuong Bui [3], Lam Dai Tran [2,4], Chuong V. Nguyen [5], Dai-Viet N. Vo [6] and Sy Trung Do [7,*]

1   NTT Hi-tech Institute, Nguyen Tat Thanh University, 300A Nguyen Tat Thanh, District 4, Ho Chi Minh City 755414, Vietnam; nguyenhuuvinh3110@gmail.com (V.H.N.); blgiangntt@gmail.com (L.G.B.)
2   Institute for Tropical Technology, Vietnam Academy of Science and Technology, 18 Hoang Quoc Viet, Cau Giay, Hanoi 10072, Vietnam; hoangth@itt.vast.vn (T.H.); trandailam@gmail.com (L.D.T.)
3   Faculty of Chemical Technology, Ho Chi Minh City University of Food Industry, 140 Le Trong Tan, Tan Phu District, Ho Chi Minh City 705800, Vietnam; phuongquynh102008@gmail.com
4   Graduate University of Science and Technology, Vietnam Academy of Science and Technology, 18 Hoang Quoc Viet, Cau Giay, Hanoi 10072, Vietnam
5   Department of Materials Science and Engineering, Le Quy Don Technical University, Hanoi 100000, Vietnam; chuongnguyen11@gmail.com
6   Faculty of Chemical & Natural Resources Engineering, University Malaysia Pahang, Lebuhraya Tun Razak, Gambang 26300, Malaysia; vietvo@ump.edu.my
7   Institute of Chemistry, Vietnam Academy of Science and Techology, 18 Hoang Quoc Viet, Cau Giay District, Hanoi 10072, Vietnam
*   Correspondence: ndtrinh@ntt.edu.vn (T.D.N.); dosyvhh@gmail.com (S.T.D.); Tel.: +84-971-275-356 (T.D.N.); +84-969-937-586 (S.T.D.)

Abstract: Mixed Ni/Fe-base metal-organic framework (Ni/Fe-MOF) with different molar ratios of Ni^{2+}/Fe^{3+} have been successfully produced using an appropriate solvothermal router. Physicochemical properties of all samples were characterized using X-ray diffraction (XRD), Raman, field emission scanning electron microscopes (FE-SEM), fourier-transform infrared spectroscopy (FT-IR), N_2 adsorption-desorption analysis, X-ray photoelectron spectroscopy (XPS), ultraviolet-visible diffuse reflectance spectra (UV-Vis DRS), and photoluminescence spectra (PL). The photocatalytic degradation performances of the photocatalysts were evaluated in the decomposition of rhodamine B (RhB) under a compact fluorescent daylight lamp. From XRD, IR, XPS, and Raman results, with the presence of mixed ion Fe^{3+} and Ni^{2+}, MIL-88B (MIL standing for Materials of Institut Lavoisier) crystals based on the mixed metal Fe_2NiO cluster were formed, while MIL-53(Fe) was formed with the presence of single ion Fe^{3+}. From UV-Vis DRS results, Ni/Fe-MOF samples exhibited the absorption spectrum up to the visible region, and then they showed the high photocatalytic activity under visible light irradiation. A Ni/Fe-MOF sample with a Ni^{2+}/Fe^{3+} molar ratio of 0.3 showed the highest photocatalytic degradation capacity of RhB, superior to that of the MIL-53(Fe) sample. The obtained result could be explained as a consequence of the large surface area with large pore volumes and pore size by the Ni^{2+} incorporating into the MOF's structure. In addition, a mixed metal Fe/Ni-based framework consisted of mixed-metal cluster Fe_2NiO with an electron transfer effect and may enhance the photocatalytic performance.

Keywords: photocatalytic decomposition of rhodamine B; MIL-53(Fe); Ni/Fe-MOF; visible light irradiation

1. Introduction

Metal-organic frameworks (MOFs), a new class of high surface area and crystalline porous materials, assemble with metal clusters and organic bridging ligands [1]. These materials have received considerable attention in recent years due to their high resistance, high surface area, large pore volume, low density, and easily tunable framework. Among the MOFs, MIL-53(Fe) 88B (MIL standing for Materials of Institut Lavoisier) have attracted extensive interest for applications in gas storage [2,3], adsorption and separation of heavy metal [4], sensors [5], and in the biomedical field such as for drug delivery [6].

Recently, to eliminate organic dyes, many approaches have been suggested including adsorption [7–10] and photodegradation [11–13]. However, the latter is of interest because this process could decompose organic dyes to CO_2, H_2O, and harmless inorganics, while the adsorption process is only capable of removing dyes from water media. MIL-53(Fe) as a catalyst carrier or modification of MIL-53(Fe) as a catalyst for chemical reactions has received research attention [14]. MIL-53(Fe) has the chemical formula of $Fe^{III}(OH)(O_2C–C_6H_4–CO_2)\cdot H_2O$, which consists of FeO_6 octahedral chains connected to benzene dicarboxylate (BDC) anions, forming a three-dimensional network with a large volume and high surface area [2,14,15]. The FeO_6 octahedral chains have the potential to act as a Lewis acid in many organic reactions [16]. Recently, MIL-53(Fe) with the potential use of FeO_6 octahedral chains has received much attention in photocatalytic degradation of many organic dyes, such as methylene blue [11,13,17], rhodamine B (RhB) [14,16,17], and p-nitrophenol [14], and has given good decomposition results. Therefore, this is a possible application direction of MIL-53(Fe) in the removal of organic dyes.

Fe-based MOFs materials have been reported as an effective photocatalyst for decomposition of organic dyes under visible light irradiation [18–22]. However, their photocatalytic performance is not as expected because of the fast recombination of photogenerated holes (h^+) and electrons (e^-), resulting in the lack of h^+ for degradation dyes [13]. To address this, various approaches have been proposed to depress the recombination process. For example, inorganic oxidants (e.g., H_2O_2, $KBrO_3$, and $(NH_4)_2S_2O_8$), which act as electron acceptors, was introduced in the photocatalytic processes, significantly enhancing the photocatalytic effect of these materials. According to research by Yuan et al. [13], H_2O_2 is an efficient electron acceptor in the photocatalytic decomposition process of organic pigments by MIL-53(Fe) under visible light irradiation. Another approach that has been developed to enhance the photocatalytic performance of MiL-53(Fe) is the designed synthesis of composite photocatalysts containing MOFs materials such as CdS/MIL-53(Fe) [23], Ni-MOFs@GO [24], Fe_3O_4/MIL-53(Fe) [14], and Fe_2O_3/MIL-53(Fe) [25]. In addition, MIL-53(Fe) that has been doped or combined with one or more metals have also attracted much attention in recent years [26–29]. For this study, Qiao Sun et al. modified the MIL-53(Fe) by adding Mn, Co, and Ni metal into the framework of MIL-53(Fe) material, which exhibited excellent catalytic performance in liquid-phase degradation of phenol [30]. Various rare-earth or transition metals that modify MOFs structures have recently been reported such as three-dimensional Ln(III)–Zn(II) heterometallic coordination polymers [31], Fe substituted Cr MIL-101 [32], Ag-doped MOF-like organotitanium polymer (Ag@NH2-MOP(Ti)) [33], Ti-doped UiO-66 [34], Eu substituted Fe MIL-53 [35], and Zn-Ln coordination polymers (Ln = Nd, Pr, Sm, Eu, Tb, Dy) [36].

In this work, we report the synthesis of Ni/Fe-MOF with different Ni^{2+}/Fe^{3+} molar ratios using the solvothermal route and their application for the degradation of RhB solution under visible light irradiation using a 40 W compact fluorescent lamp. To illustrate our method for the synthesis of Ni/Fe-MOF, we have selected the preparation of the MIL-53(Fe) structure, which consists of FeO_6 octahedral chains connected to BDC anions. Thanks to the presence of Ni^{2+} ions in the reaction solution, MIL-88B crystals were formed with neutral mixed-metal clusters (Fe_2NiO) connected via BDC anions. This structure is similar to the MIL-88B structure consisting of the trinuclear oxo-centered iron cluster (Fe_3O) [27,28]. However, our bimetallic metal MOF products were expected to exhibit an excellent adsorption capacity and photocatalytic activity in comparison to the original single metal MOFs.

The advantage of selecting MOF material containing Fe and Ni is due to the low cost, non-toxicity, and natural abundance of these two transition metal oxides. In addition, the MOF material is also capable of improving the separation efficiency of electron–hole pairs when Ni is incorporated into the structure of materials [37,38]. The structure, morphology, and optical properties of the obtained photocatalysts have been characterized using X-ray diffraction (XRD), Raman, field emission scanning electron microscopes and energy-dispersive X-ray spectrometer (FE-SEM/EDS), fourier-transform infrared spectroscopy (FT-IR), N_2 adsorption-desorption analysis, X-ray photoelectron spectroscopy (XPS), ultraviolet-visible diffuse reflectance spectra (UV-Vis DRS), photoluminescence (PL) spectra and nitrogen physisorption measurements (BET). Besides, to obtain the optimal reaction conditions for the RhB photodecomposition, the effect of the initial RhB concentration and pH on the degradation of RhB was also investigated in detail.

2. Results and Discussion

2.1. Physical Properties of MIL-53(Fe) and Ni-Doped MIL-53(Fe)

2.1.1. XRD Analysis

Figure 1 presents the XRD diffraction patterns of the MIL-53(Fe) and Ni/Fe-MOF samples isolated from dimethylformamide (DMF) and H_2O. In patterns of MIL-53(Fe) samples (Figure 1A, curve a), the main diffraction peaks that appeared at 2θ of 9.1°, 9.4°, 14.1°, 16.5°, and 18.8° are similar to those previously reported for MIL-53(Fe) isolated from DMF [2,11,39]. In patterns of Ni/Fe-MOF samples (Figure 1A, curves b–e), the main diffraction peaks that appeared around 2θ of 7.3°, 8.9°, 9.3°, 9.9°, 16.8°, 18.7°, 17.7°, 20.1°, and 21.9° are similar to those previously reported for MIL-88B isolated from DMF. Notably, the diffraction peak at a 2θ of 7.3° observed in the XRD patterns of Ni/Fe-MOF samples increased in intensity as the molar ratio of Ni^{2+}/Fe^{3+} increased from 0.1 to 0.7. With the presence of Ni^{2+} in the reaction solution, MIL-88B crystals were made up and the crystallinity of the material increased. This observation might be attributed to the fact that the structure formation of Ni/Fe-MOF was significantly influenced by the presence of Ni^{2+} in the reaction solution. In addition, no other diffraction peak associated with nickel oxides, iron oxides, or other impurities could be detected, demonstrating the high purity of the samples.

XRD patterns of the MIL-53(Fe) and Ni/Fe-MOF samples isolated from H_2O (Figure 1B) showed the rugged background and weak intensities; however, the main diffraction peaks still maintained the same structure as in Reference [4]. The difference in XRD patterns of samples isolated from DMF and water may attribute to the breathing behavior of MIL-53(Fe) and MIL-88B, which has been well documented by Alhanami et al. [15]. Moreover, MIL-53(Fe)·H_2O sample essentially shows a noncrystalline phase similar to those for MIL-53(Fe)·DMF. They can be explained by the effect of the synthesis temperature on the structure formation of MIL-53(Fe). Pu et al. demonstrated that iron ion and H_2BDC could not coordinate successfully under a low temperature (100 °C), and therefore the MIL-53(Fe) crystal structure could not fully develop [40]. However, the Ni/Fe-MOF samples still show a high crystalline phase under low synthesis temperatures. Again, these results indicate that the presence of a mixed metal ion (Ni^{2+} and Fe^{3+} ion) did have a significant influence on the formation of Ni/Fe-MOF crystal structure, in which a Ni^{2+} and Fe^{3+} ion can coordinate with H_2BDC to form MIL-88B crystals instead of MIL-53(Fe) crystals.
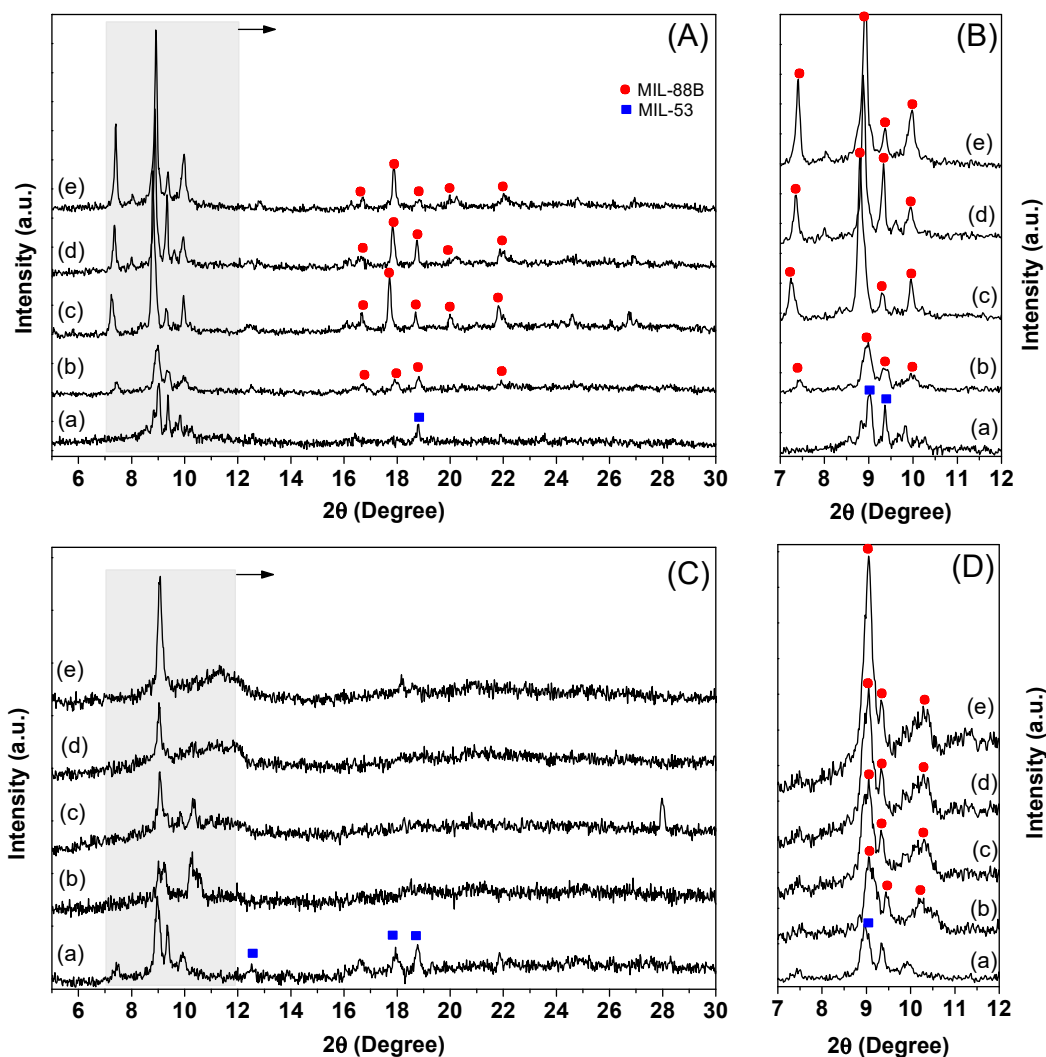
Figure 1. XRD patterns of as-prepared MIL-53(Fe) and Ni-MIL-53(Fe) crystals isolated from DMF (**A**,**B**) and H$_2$O (**C**,**D**): MIL-53(Fe) (a), Ni/Fe-MOF-0.1 (b), Ni/Fe-MOF-0.3 (c), Ni/Fe-MOF-0.5 (d), and Ni/Fe-MOF-0.7 (e).

2.1.2. FT-IR Spectra

FTIR spectroscopic studies were performed for all samples in the wave range of 400–4000 cm^{-1}, as shown in Figure 2. As shown in Figure 2A,C, strong vibrational bands around 1657, 1601, 1391, 1017, and 749 cm^{-1}, which are attributed to υ(C=O), υas(OCO), υs(OCO), υ(C–O), and δ(C–H) vibrations confirms the presence the bridge coordination mode of metal carboxylates in the MOF structures [4,25,30]. No band at 1700 cm^{-1} was found, implying no free H$_2$BDC [27]. The band characteristics of DMF (1657 cm^{-1}) and H$_2$O (3387 cm^{-1}) were present in the samples MIL-53(Fe)·DMF, Ni/Fe-MOF·DMF, MIL-53(Fe)·H$_2$O and Ni/Fe-MOF-x·H$_2$O, respectively [27].

At lower frequencies (Figure 2B), vibrational bands around 750 cm^{-1}, 690 cm^{-1}, and 660 cm^{-1} represent the C–H vibration, C=C stretch, OH bend, and OCO bend, respectively, were found, implying the presence of the vibrations of the organic ligand BDC [27]. Figure 2B also shows that the strong band at 547 cm^{-1} in all samples could be attributed to Fe–O vibrations or Ni–O vibrations [41]. The band around 625 cm^{-1} belongs to the Fe$_3$O vibration, which was observed in MIL-53(Fe) and Ni-Ni/Fe-MOF-0.1 samples. The weak band around 720 cm^{-1} is related to the Fe$_2$NiO vibration, which was observed in Ni/Fe-MOF-x samples [27]. These results reaffirmed that Ni^{2+} and Fe^{3+} ions can coordinate with H$_2$BDC to form MIL-88B crystals.
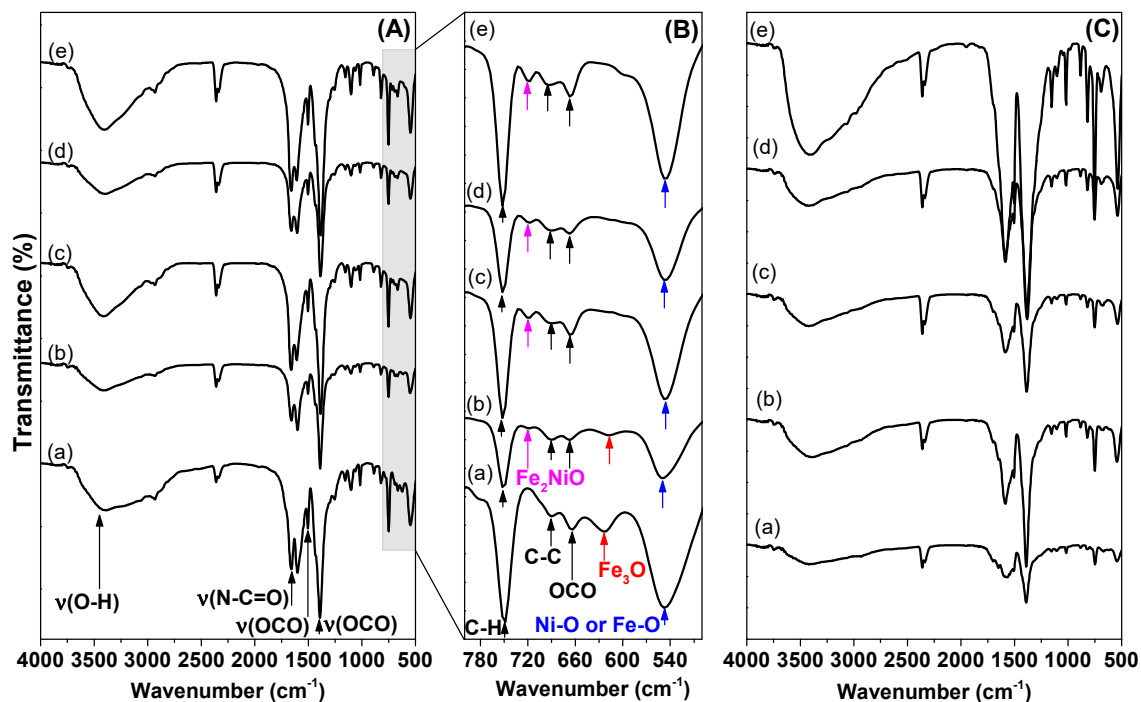
Figure 2. FT-IR spectra of as-prepared MIL-53(Fe) and Ni/Fe-MOF crystals isolated from DMF (**A**,**B**) and H$_2$O (**C**): MIL-53(Fe) (a), Ni/Fe-MOF-0.1 (b), Ni/Fe-MOF-0.3 (c), Ni/Fe-MOF-0.5 (d), and Ni/Fe-MOF-0.7 (e).

2.1.3. Raman Spectra

Samples were analyzed using Raman spectroscopy using an excitation wavelength at 633 nm and spectra recorded at a wavenumber range of 100–900 cm^{-1}, as shown in Figure 3. According to previous studies, the BDC bridge in MOFs has Raman-active modes: the symmetric vibration modes (vs. (COO)) and asymmetric vibration (vas (COO)) of the carboxylate group (1445 cm^{-1} and 1501 cm^{-1}), the vibration of the C–C bond between the benzene ring and the carboxylate group (1140 cm^{-1}), and the external plane deformation of the C–H link (865 cm^{-1} and 630 cm^{-1}) [28]. As seen in Figure 3, the presence of a BDC linker was also observed in all samples, and no Raman signals corresponding to nickel oxides, iron oxides, or other impurities were found on any of the samples, which is consistent with the results of the XRD patterns. Notably, the Raman signal corresponding to the symmetric vibration (vs. (OCO)) of the carboxylate group showed a shift to a lower wavenumber and the peak split into two peaks corresponding to an increase of the Ni^{2+}/Fe^{3+} molar ratio. This result was due to the change in the charge distribution in the organic bridge when they were coordinated with different metal ions (Figure 3B). Ionic Ni^{2+} has a smaller nuclear charge and a larger ionic radius than Fe^{3+} ($r_{Ni^{2+}}$ = 0.69 Å and $r_{Fe^{3+}}$ = 0.55 Å) [42]. Therefore, Ni^{2+} creates a weaker coordinated link with the OCO group on the organic bridge than Fe^{3+}, thus the symmetric vibration (vs. (OCO)) of the carboxylate group when forming coordinated bonds with Ni^{2+} moves to a lower wavenumber than Fe^{3+} [43]. This result is commensurate with the XRD and IR results for Ni/Fe MOF.
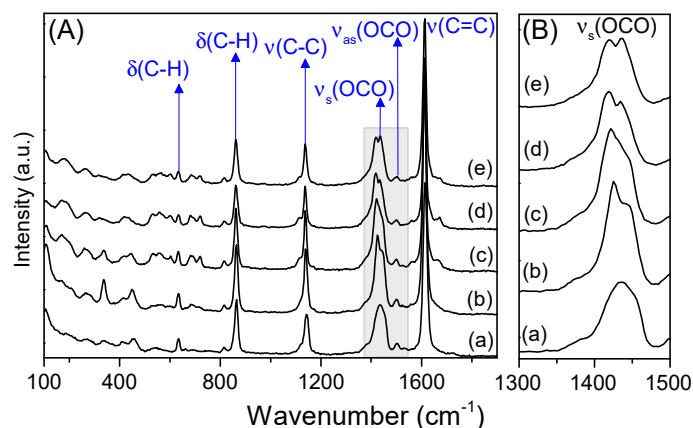
Figure 3. Raman spectra of as-prepared MIL-53(Fe) and Ni/Fe-MOF crystals isolated from DMF (**A**): MIL-53(Fe) (a), Ni/Fe-MOF-0.1 (b), Ni/Fe-MOF-0.3 (c), Ni/Fe-MOF-0.5 (d), and Ni/Fe-MOF-0.7 (e), and enlarged Raman spectra around 1450 cm^{-1} (**B**).

2.1.4. FE-SEM/EDS Analysis

Figure 4 displays SEM images and EDS spectra of the as-prepared MOF samples. As shown in Figure 4, the morphologies and shapes of MOF samples varied according to the molar ratio of Ni^{2+}/Fe^{3+}. MIL-53(Fe) sample mostly had amorphous nanoparticles (Figure 4(a1,a2)), which is in good agreement with the results of XRD patterns with a poor crystallinity. When the molar ratio of Ni^{2+}/Fe^{3+} was set to 0.1, the crystals of Ni/Fe-MOF-0.1 were not homogeneous with different shapes and sizes (Figure 4(b1,b2)). A mixture of octahedral and hexagonal bipyramidal shapes, and nanoparticles, were perceived when the molar ratio of Ni^{2+}/Fe^{3+} (0.3–0.7) was increased further. However, these octahedral and hexagonal bipyramidal shapes collapsed with cracks on the crystal surface. These results, along with the XRD, IR, and Raman results above, indicate that a mixed-metal Ni/Fe-MOF was successfully synthesized using the solvothermal method.

Moreover, to confirm the molar ratio of Ni^{2+}/Fe^{3+} in the Ni/Fe-MOF samples in comparison to the theoretical value, EDS was also conducted. The result from the EDS spectrum of the obtained MIL-53(Fe) sample (Figure 4(a3)) showed the coexistence of C, O, Fe, and Cl. The presence of Cl may have been due to the $FeCl_3$ precursor, further confirming that the MIL-53(Fe) crystal structure could not fully develop at a low temperature (100 °C). The EDS spectra of the Ni/Fe-MOF samples (Figure 4(b3,c3,d3,e3)) revealed that these samples contained C, O, Fe, and Ni. However, the existence of Cl was still observed in the Ni/Fe-MOF-0.1 sample. The molar ratio of Ni^{2+}/Fe^{3+} of Ni/Fe-MOF-0.1, Ni/Fe-MOF-0.3, Ni/Fe-MOF-0.5, and Ni/Fe-MOF-0.7, obtained using EDS analysis, was 0.16, 0.30, 0.48, and 0.66, respectively. In addition, the map of Fe, O, C, and Ni is shown in Figure S1, which indicates that they were uniformly distributed over the MOF surface.
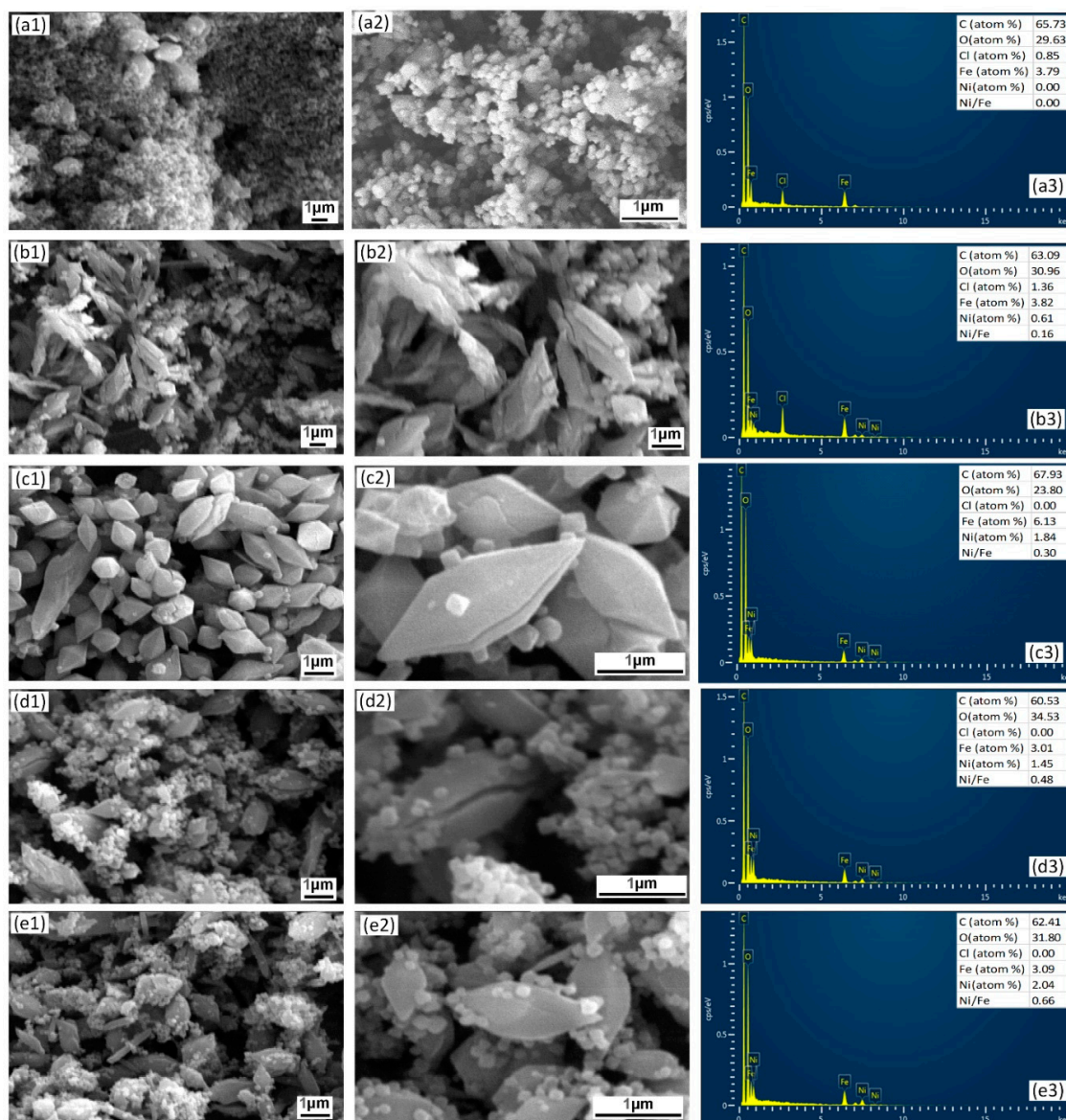
Figure 4. SEM images (1, 2) and EDS patterns (3) of as-prepared MIL-53(Fe) and Ni/Fe-MOF crystals isolated from DMF: MIL-53(Fe) (**a**), Ni/Fe-MOF-0.1 (**b**), Ni/Fe-MOF-0.3 (**c**), Ni/Fe-MOF-0.5 (**d**), and Ni/Fe-MOF-0.7 (**e**).

2.1.5. XPS Spectra

To analyze the chemical states of Ni and Fe in the Ni/Fe MOF structure, XPS spectroscopy was carried out. As illustrated in Figure 5A, the wide-scan XPS spectra of MIL-53(Fe)·H_2O possesses the characteristic peaks of C, O, Fe, and Cl, while Ni/Fe-MOF-0.3.H_2O contained C, O, Fe, and Ni. Based on the XPS analysis, the Ni/Fe-MOF-0.3 had a surface molar ratio of Ni^{2+}/Fe^{3+} of 0.26, which approximates the EDS results above. Besides, N was not detected in either sample, indicating that the DMF solvent was sufficiently eliminated from the MOFs.

Figure 5B shows the C 1s XPS spectra of MIL-53(Fe)·H_2O and Ni/Fe-MOF-0.3·H_2O samples. Both spectra were fitted into three peaks at a binding energy (BE) of 285.01, 288.9, and 291.7 eV, which could be assigned to the carbon components on the phenyl and the carboxylate groups of the BDC linkers [30,40,44–46]. The O 1s XPS spectra (Figure 5C) could also be fitted into three peaks, which are (i) the peak at 533.8 eV corresponding to the O components on C=O/H_2O, (ii) the peak at 532.3 eV attributed to the O components on the BDC linkers, and (iii) the peak at 530. 5 eV was assigned to the

O components on the Fe–O bonds (for MIL-53(Fe) sample) or Fe_2NiO clusters (for Ni/Fe-MOF-0.3 sample). These results further confirmed the coordination between the metal ion (Ni^{2+} and/or Fe^{3+}) and BDC linkers, which is commensurate with the XRD, IR, and Raman results above.
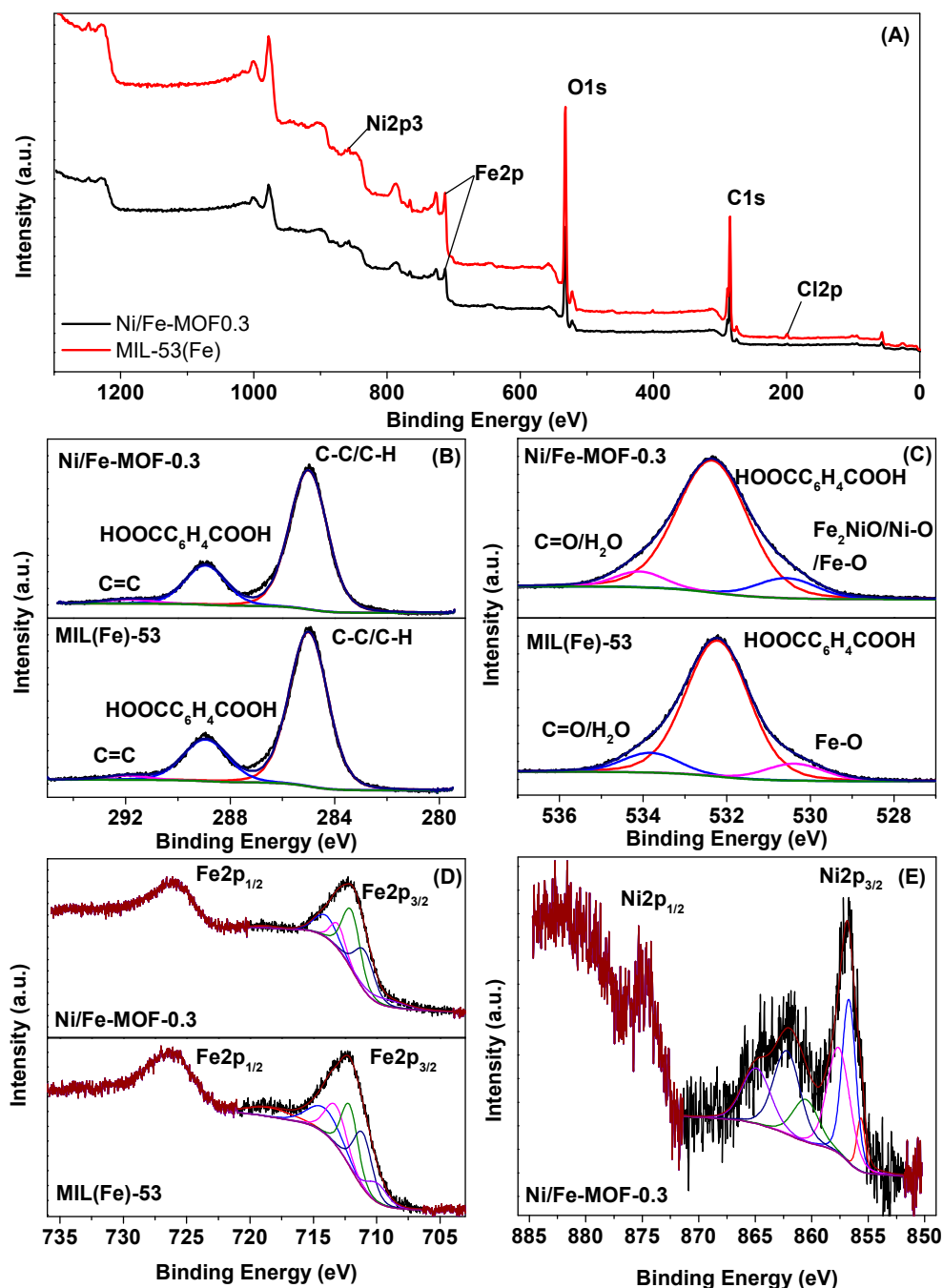
Figure 5. Full scan (**A**), C1s (**B**), O1s (**C**), Fe2p (**D**), and Ni2p (**E**) XPS spectra of MIL-53(Fe) and Ni/Fe-MOF-0.3.

The Fe 2p high-resolution XPS spectrum of MIL-53(Fe) sample (Figure 5D) displays two main peaks that were indexed to Fe 2p1/2 (712.4 eV) and Fe2p3/2 (726.1 eV). The splitting energy of the 2p doublet was 13.7 eV, implying that the valence state of Fe was +3 [4,23,44]. Similarly, the valence state of Fe in the Ni/Fe MOF structure was also +3 because the splitting energy between Fe 2p1/2 (712.9 eV) and Fe 2p3/2 (726.2 eV) was 13.3 eV. To further confirm the valence state of Fe in both of these samples, the Fe 2p3/2 peak was fitted into six peaks including Gupta and Sen (GS) multiples,

surface structures, and shake-up-related satellites [28,47,48]. The fitting results, as shown in Figures S6 and S7, were indexed well with Fe^{3+} GS multiplets, which indicated that the valence state of Fe in the MIL-53(Fe) and Ni/Fe MOF structure was +3. In the high-resolution XPS spectrum of Ni 2p (Figure 4e), we observed the BE of the Ni 2p3/2 (857.2 eV) and Ni 2p1/2 (874.8 eV) core-level peaks with the doublet separation of 17.6 eV, implying that the valence state of Ni was +2 [49,50].

2.1.6. N_2 Adsorption/Desorption

The specific surface area and porous structure of MIL-53(Fe) and Ni/Fe-MOF crystals isolated from DMF and H_2O were determined using N_2 adsorption–desorption isotherms at 77 K. The N_2 adsorption–desorption isotherms, as shown in Figure 6A, displayed an intermediate mode between type I and type IV, which was associated with mesoporous and microporous materials, respectively [51]. The Brunauer–Emmett–Teller (BET) surface area, pore volume, and pore width of MIL-53(Fe) and Ni/Fe-MOF-0.3 samples are shown in Table 1. The MIL-53(Fe)·H_2O, MIL-53(Fe)·DMF, Ni/Fe-MOF-0.3.H_2O, and Ni/Fe-MOF-0.3.DMF had specific surface areas of 158, 300, 247, and 480 m^2/g, respectively (Table 1). The mesopore size distribution curve of samples calculated using the Barrett–Joyner–Halenda (BJH) model is shown in Figure 6B. The MIL-53(Fe)·H_2O and MIL-53(Fe)·DMF sample was non-porous, whereas Ni/Fe-MOF-0.3·H_2O, and Ni/Fe-MOF-0.3·DMF showed a pore size centered at about 3.8 nm and 21.4 nm, respectively. Therefore, compared with MIL-53(Fe), Ni/Fe-MOF-0.3 showed a higher value in the specific surface areas. In addition, the higher surface area and micropore volume for samples isolated from DMF, as compared with samples isolated from H_2O, was due to the reversible breathing behavior of these materials, which was dependent on the molecule present inside their pores, where the pores were opened in the presence of DMF and closed in the presence of H_2O [27,28,52]. The formation of porous material for Ni/Fe-MOF-0.3 could be explained by the formation of Fe_2NiO cluster in the Ni/Fe-MOF structure, which could affect the reversible breathing behavior of these materials. MIL-88B(Fe) crystals with trinuclear metal clusters were known as non-porous materials due to the need for compensating the anion inside their porous system [28,53]. Do and coworkers demonstrated that MOF structure with the presence of Fe_2NiO cluster as nodes in the MIL-88B framework avoids the compensating anion [27,28], which results in the formation of porous material for Ni/Fe-MOF-0.3. In addition, the cracks on the crystal surface of Ni/Fe-MOF-0.3 (Figure 4) could also partly create the characteristics of microporous or mesoporous materials for this sample.

Table 1. Specific surface area and porosity of MiL-53(Fe) and Ni/Fe-MOF samples.

Samples	Specific Surface Area (m^2/g)	Micropore Volume ($\times 10^{-3}$ cm^3/g)	Mesopore Volume ($\times 10^{-3}$ cm^3/g)	Average Pore Width (nm)
MIL-53(Fe)·DMF	300	128	97	13
MIL-53(Fe)·H_2O	158	65	59	11
Ni/Fe-MOF-0.3·DMF	480	212	128	8
Ni/Fe-MOF-0.3·H_2O	247	94	271	13
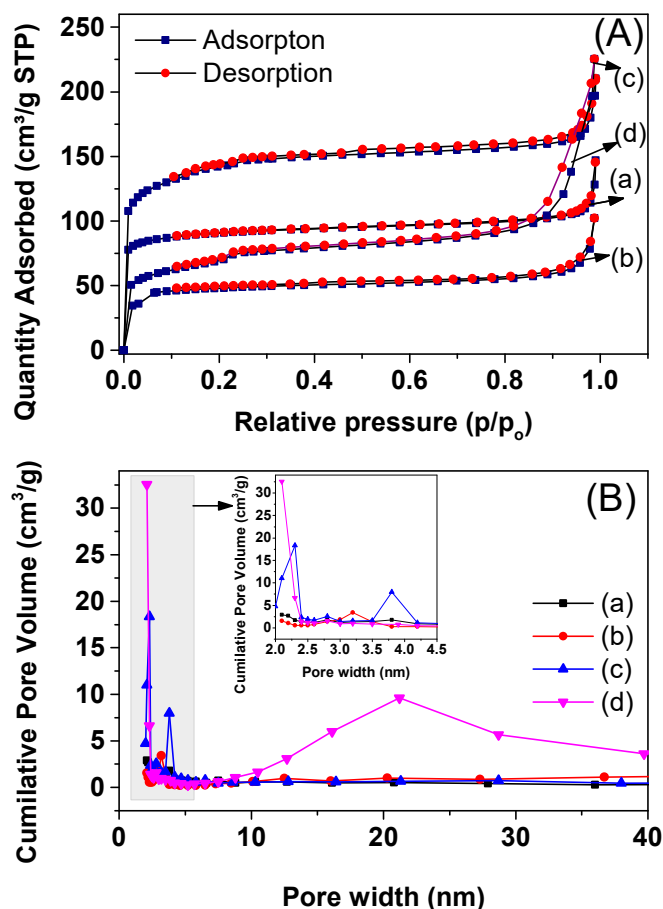
Figure 6. N_2 adsorption–desorption isotherms (**A**) and pore size distributions (**B**) of the synthesized samples: MIL-53(Fe)·DMF (a), MIL-53(Fe)·H_2O (b), Ni/Fe-MOF-0.3·DMF (c), and Ni/Fe-MOF-0.3·H_2O (d).

2.1.7. UV-Vis Spectra

The light absorption properties of the material were studied through the UV-Vis-DRS spectra. The UV-Vis-DRS spectrum of the material is shown in Figure 7. For washing samples with DMF (Figure 7A), MIL-53(Fe)·DMF gave strong absorption bands in the wavelength range of 200 to 400 nm. The strong absorption bands at 256 to 310 nm could be due to the transfer of the charge from the oxygen center of the organic bridge to the metal center in the octahedral FeO_6 structure [17,54]. The band at 350 to 500 nm was due to the shift of d–d (6A1g → 4A1g + 4Eg (G)) of Fe^{3+} in the MIL-53(Fe) structure [14,27]. The main absorption edge (λ, nm) of the MIL-53(Fe)·DMF was 478 nm, corresponding to the bandgap energy $E_g = 2.59$ eV ($E_g = 1240/λ$). This result is in accordance with previous reports [44,55]. When the MIL-53(Fe) was modified with Ni, the material have the decreased absorption in the wavelength range from 200 to 500 nm, and the absorption spectrum extended in the range from 250 to 800 nm, so it was difficult to determine the absorption of the material accurately. When the material was washed with water (Figure 7B), the modified material had an increased absorption in the wavelength range from 200 to 400 nm, and the absorption intensity was higher and broader in the visible light region as compared to the modified sample washed with DMF. As the material was washed with water, there was a structural change between the large pore and the narrow pore caused by the "breathing" effect when the material absorbed the water molecules inside the pore. This phase transformation of the structure led to a change in the electronic structure [56], and subsequently, a change in the absorption spectrum of the material and decreasing E_g. For Ni/Fe-MOF-0.1·H_2O, Ni/Fe-MOF-0.3·H_2O, and Ni/Fe-MOF-0.5·H_2O samples, the absorption intensity in the visible light region and the absorption band of the material shifted to a wavelength longer than for MIL-53(Fe)·H_2O. As absorption in the visible light increased, the visible

light energy could be used more efficiently, thus contributing to the increased photocatalytic efficiency of the material. The absorption edges of MIL-53(Fe)·H_2O, Ni/Fe-MOF-0.1·H_2O, Ni/Fe-MOF-0.3·H_2O, Ni/Fe-MOF-0.5·H_2O, and Ni/Fe-MOF-0.7·H_2O were 504, 553, 532, 513, and 516 nm (Figure S2), corresponding to the optical bandgap of 2.46, 2.24, 2.33, 2.42, and 2.40 eV, respectively. These results provided a potential photoreactivity of MIL-53(Fe) and Ni/Fe-MOF samples in the visible light range.
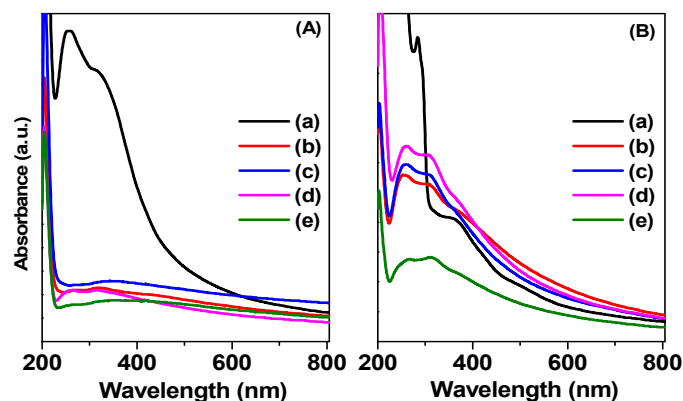
Figure 7. UV-Vis DRS spectra of as-prepared MIL-53(Fe) and Ni-MIL-53(Fe) crystals isolated from DMF (**A**) and H_2O (**B**): MIL-53(Fe) (a), Ni/Fe-MOF-0.1 (b), Ni/Fe-MOF-0.3 (c), Ni/Fe-MOF-0.5 (d), and Ni/Fe-MOF-0.7 (e).

2.1.8. PL Spectroscopy

PL spectra of MIL-53(Fe) and Ni/Fe-MOF samples were recorded at room temperature and are shown in Figure 8. When the MIL-53(Fe) sample was excited by a 320 nm laser, its emission spectrum showed a strong emission range of 350 to 500 nm and a weak emission range of 570 to 750 nm. In comparison, the intensity of Ni/Fe-MOF samples was significantly lower than that of the MIL-53(Fe) sample because of the presence of the Ni_2FeO cluster in the structure of the Ni/Fe-MOF crystal. These results demonstrated that electron–hole recombination could be inhibited in the Ni/Fe-MOF, resulting in the improvement of photocatalytic performance. PL spectra, along with the UV-Vis DRS result, could satisfy the prerequisite for visible-light photocatalysis.
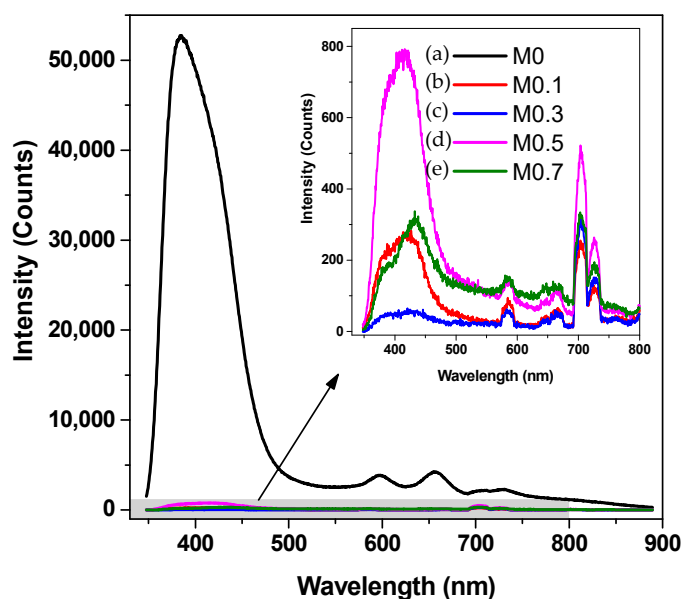
Figure 8. PL spectra of as-prepared MIL-53(Fe) (a), Ni/Fe-MOF-0.1 (b), Ni/Fe-MOF-0.3 (c), Ni/Fe-MOF-0.5 (d), and Ni/Fe-MOF-0.7 (e).

2.2. Photocatalytic Activities

2.2.1. RhB Removal by MIL-53(Fe) and Ni-MIL-53(Fe)

The photocatalytic activities of MIL-53(Fe) and Ni/Fe-MOF-x photocatalysts were evaluated in the liquid-phase photodegradation of RhB dye under visible light irradiation. Figure 9 displays the changes of RhB concentrations via adsorption and photocatalytic degradation under different experimental conditions. As shown in Figure 9, a negligible degradation of RhB concentrations was observed in the several blank runs including RhB/H_2O_2/Dark, RhB/H_2O_2/Light, and RhB/Dark systems, proving the stability property of RhB under visible light irradiation of compact fluorescent light. Also, as shown in Figure 9A, after 180 min adsorption (in the dark), 16% and 51% RhB were removed in the presence of MIL-53(Fe) (MIL-53(Fe)/Dark system) and Ni/Fe-MOF-0.3 (Ni/Fe-MOF-0.3/Dark system), respectively. The higher adsorption capacity of the Ni/Fe-MOF-0.3 sample was due to its higher surface area (247 m^2/g for Ni/Fe-MOF-0.3 and 158 m^2/g for MIL-53(Fe)). In addition, there was no significant difference in the removal of RhB concentration in the two adsorption experiments with the presence of H_2O_2 (MIL-53(Fe)/H_2O_2/Dark and Ni/Fe-MOF-0.3/H_2O_2/Dark systems) and the absence of H_2O_2 (MIL-53(Fe)/Dark and Ni/Fe-MOF-0.3/Dark systems). Therefore, our photocatalytic experiments do display the presence of a Fenton reaction.
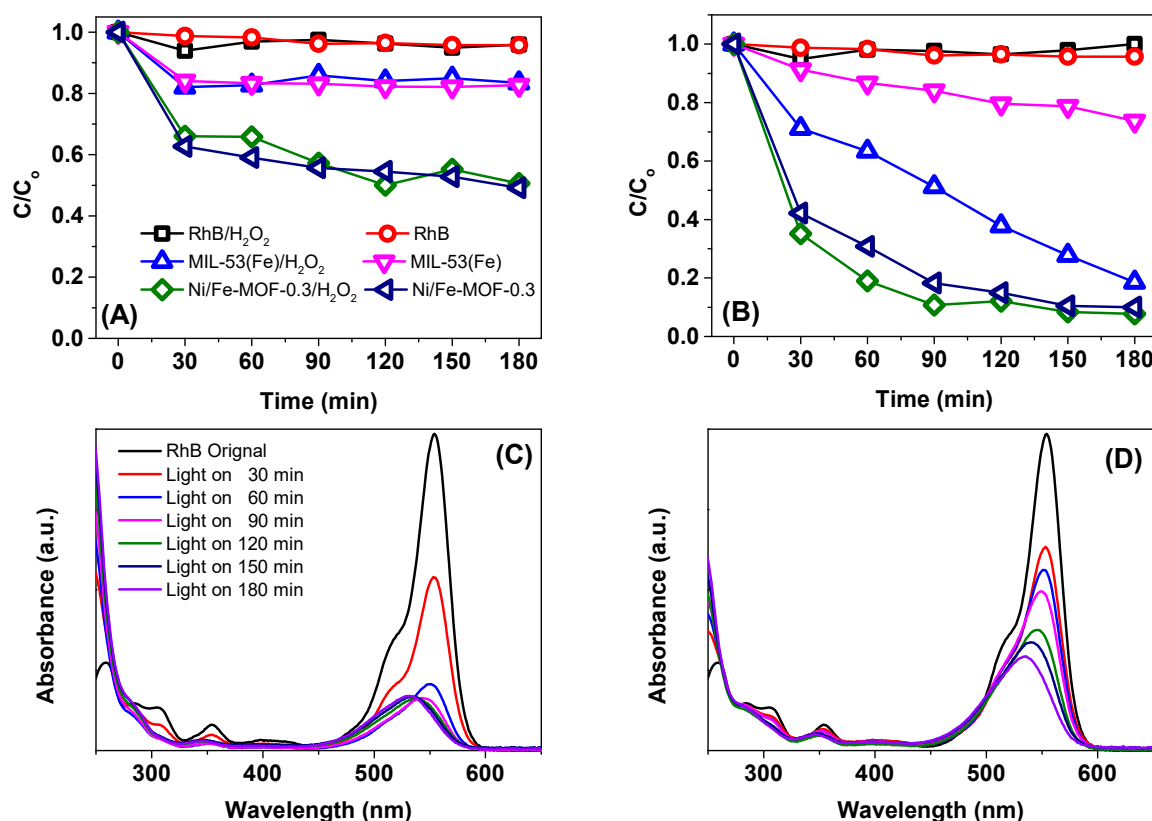
Figure 9. Adsorption (**A**) and photodegradation (**B**) of RhB under different conditions over MIL-53(Fe) and Ni/Fe-MOF-0.3, and UV-Vis spectral of RhB solution separated from the Ni/Fe-MOF-0.3/ Light/H_2O_2 catalytic system (**C**) and MIL-53(Fe)/Light /H_2O_2 catalytic system (**D**).

Under visible light irradiation, the presence of MIL-53(Fe) could enhance the degradation efficiency of RhB up to 81.46% using a photolysis process in MIL-53(Fe)/Light/H_2O_2 catalytic system (Figure 9B). For the Ni/Fe-MOF-0.3/Light/H_2O_2 catalytic system, the degradation efficiency of RhB was remarkably enhanced where about 91.14% RhB removal was achieved (Figure 9B). The higher photocatalytic activity of the Ni/Fe-MOF-0.3 sample as compared with MIL-53(Fe) could also be indicated by the change of the UV-Vis absorption spectra of the solution in the course of the RhB

degradation (Figure 9C,D). As seen in Figure 9C,D, the primary absorption band, which could be attributed to RhB, shifted from 554 to 500 nm in a step-wise manner. This change could be reasonably assigned to the removal of ethyl groups one by one in this reaction, which is in good agreement with the previous literature. The photodegradation of RhB over MIL-53(Fe) and Ni/Fe-MOF-0.3 photocatalysts approximately followed a pseudo-first-order kinetics model: $\ln(C_o/C) = k_{obs}t$ [57–59]. The presence of Ni/Fe-MOF-0.3 promoted the photodegradation rate; the rate constants were 8.88×10^{-3} min^{-1} for MIL-53(Fe) and 11.15×10^{-3} min^{-1} for Ni/Fe-MOF-0.3.

To investigate the role of H_2O_2 on the photocatalytic performance of MIL-53(Fe) and Ni/Fe-MOF photocatalysts, the photocatalytic processes with the presence and absence of H_2O_2 were conducted in parallel (Figure 9B). After 180 min of irradiation, the degradation rate of RhB over MIL-53(Fe)/Light/H_2O_2 and MIL-53(Fe)/Light process was 81.46% and 27.60%, respectively. Only MIL-53(Fe) with the absence of H_2O_2 exhibits the low efficiency of RhB photodegradation due to the fast electron-hole recombination, which is in good agreement with the previous literature [13,17]. For the MIL-53(Fe)/H_2O_2/Light process, H_2O_2 acted as an electron acceptor, resulting in the suppression of charge recombination; therefore, the rate for RhB decomposition could be significantly enhanced, as was demonstrated by Du et al. [13]. Similarly, Ai et al. also showed that the enhancement of MI-53(Fe) photocatalytic performance could be due to the synergistic effects of the combination of MIL-53(Fe) and H_2O_2 under visible light irradiation [17]. Interestingly, the effect of H_2O_2 on the photocatalytic performance of the Ni/Fe-MOF photocatalyst showed a considerable difference. The Ni/Fe-MOF sample could degrade more than 90% of the initial RhB content regardless of the presence or absence of H_2O_2.

The superior catalytic performance of the Ni/Fe-MOF sample could be explained by the formation of the mixed metal cluster Fe_2NiO in the Ni/Fe-MOF framework. According to recent reports, the Fe-based framework (MIL-101, MIL-100, MIL-88, and MOF-235), containing single metal cluster Fe_3-μ_3-oxo clusters with small particle sizes, are proposed as a visible light photocatalyst [44,60–63]. The reaction mechanism of these materials have been reported based on semiconductor theory and previous reports [61–64]. Particularly, when the surface of MOFs material absorbs photons ($E_{photons} \geq E_g$), the electrons (e^-) in the valence band (VB) will be excited to the conduction band (CB), leaving the holes (h^+) in the VB. These photogenerated e^-–h^+ pairs may be further involved in the following three processes: (i) successfully migration to the surface of MOFs, (ii) being captured by the defect sites in bulk and/or on the surface region of semiconductor, and (iii) recombining and releasing the energy in the form of heat or a photon. Then, the h^+ can accept electrons and induce water molecules to generate hydroxyl radicals (•OH), which exhibit a high oxidation ability to decompose the organic dyes. However, there is a recombination of excessive electrons and holes, resulting in the restricted photocatalytic activity of this material. In our study, mixed a metal Fe/Ni-based framework that consists of a mixed-metal cluster Fe_2NiO with electron transfer effect may enhance the photocatalytic performance [45,61,65].

Besides, a mixed metal Fe/Ni-based framework that consists of the mixed-metal cluster Fe_2NiO possesses large pores and a high surface area, as compared with a single metal Fe-based framework; therefore, Ni/Fe-MOF exhibited a high adsorption capacity of RhB and high photocatalytic activity in RhB degradation. XRD patterns of Ni/Fe-MOF-0.3 before and after reactions were shown in Figure S3 (SI file). As shown in Figure S3, there was no apparent difference in the crystal structure. This result indicated that the crystal structure of the material did not change after the photocatalytic reaction.

2.2.2. Effect of Initial Dye Concentration, Initial Solution pH, and the Molar Ratio of Ni^{2+}/Fe^{3+} on the Degradation of RhB

The effect of initial dye concentration on the degradation of RhB over the Ni/Fe-MOF-0.3/Light/H_2O_2 system was evaluated (Figure 10A). As shown in Figure 10A, the degradation efficiency of RhB was slightly decreased when increasing the initial dye concentration from 1×10^{-5} to 4×10^{-5} M. This was mainly because of the increase of the dye molecules around the active sites leading to inhibiting the penetration of light to the surface of the catalyst [66].
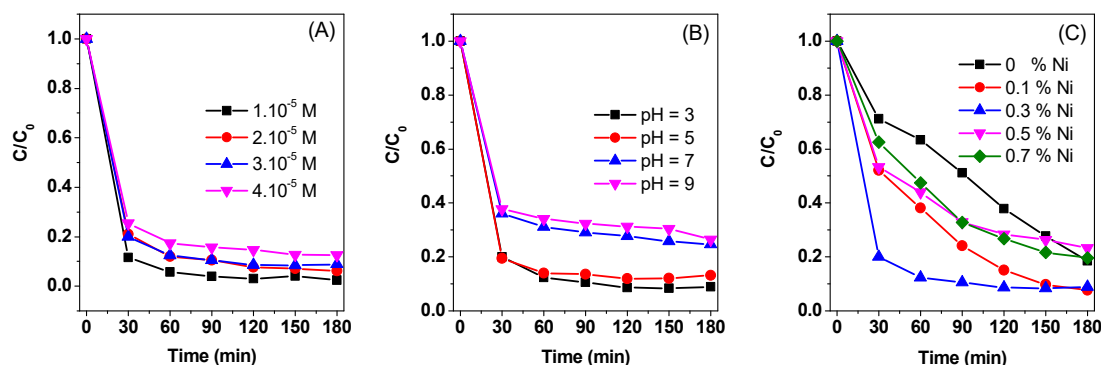
Figure 10. Effect of initial dye concentration (**A**), initial solution pH (**B**), and the molar ratio of Ni^{2+}/Fe^{3+} (**C**) on the degradation of RhB.

The effect of the initial pH on the degradation of RhB on the degradation of RhB over Ni/Fe-MOF/Light/H_2O_2 system was also investigated. The pH of the initial solution was selected as follows: 3, 5 (acidic), 7 (neutral), and 9 (basic). At different pH conditions, the Ni/Fe-MOF-0.3 remained most effective when it came to removing RhB. The RhB removal efficiency peaked at the solution pH of 5 and decreased with increasing pH thereafter (Figure 10B). This result could be explained by the fact that when the pH exceeded the isoelectric point of the material, they were negatively charged. In addition, the RhB used in this experiment was a cationic color such that the material would absorb the color gradually from pH 5 to 9. As the adsorption increased, the color molecules would shield the catalytic surface, which prevented light from irradiating on the catalyst surface, thus decreasing photocatalytic activity and reducing color removal. The pH at the isoelectric point or point of zero charge-pzc of the material was an important parameter for evaluation of the acidity/basicity and the surface charge of the adsorbent in solution. The determination of pHzpc was carried out according to our previously published study [67–69], as follows: Photocatalysts (20 mg) was added to flasks containing 100 mL of KCl 0.1 M at different initial pH values (pH_i = 2, 4, 6, 8, 10, and 12). The solutions were shaken in the shaker for 24 h, and then solids were removed from the mixture by centrifugation at 4000 rpm for 15 min. The final pH of the solution (pH_f) is measured using a pH meter. The curve was plotted via pH_f against the pH_i, and the pHpzc was calculated at pH_i = pH_f. As shown in Figure 11A,B, the pH_{pzc} values of the MIL-53(Fe) and Ni/Fe-MOF-0.3 were approximately equal and were within the pH range of 4.1–4.2.
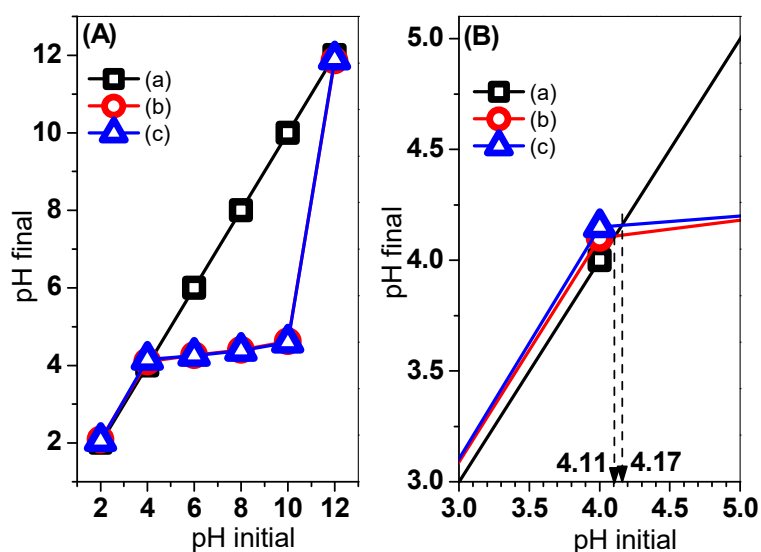
Figure 11. Measurement of pHzpc: the initial versus final pH plot: pH initial (a), pH initial-MIL-53(Fe) (b), and pH initial-Ni/Fe-MOF-0.3 (c) (**A**) and enlarged pH initial from 3 to 5 (**B**).

The degradation results of the different molar ratios of Ni^{2+}/Fe^{3+} in the samples are shown in Figure 10C, where the best performance was obtained with the Ni/Fe-MOF-0.3 sample, followed by the Ni/Fe-MOF-0.1 and Ni/Fe-MOF-0.7 samples. The Ni/Fe-MOF-0.5 sample showed the lowest catalytic activity among all the Ni/Fe-MOF catalysts. This result indicated that the different molar ratio of Ni^{2+}/Fe^{3+} had a significant impact on the photocatalytic performance of Ni/Fe-MOF samples, which may be conducive to the structure and morphology formation of Ni/Fe-MOF.

3. Experimental

3.1. Materials

1,4-Benzenedioic acid (H_2BDC, 98%) and RhB ($\geq$95%) were purchased from Sigma-Aldrich (St. Louis, MO, USA). Iron(III) chloride hexahydrate ($FeCl_3 \cdot 6H_2O$, 99%), nickel(II) nitrate hexahydrate ($Ni(NO_3)_2 \cdot 6H_2O$, 99%), *N,N*-dimethylformamide (DMF, 99%), ethanol, and hydrogen peroxide (H_2O_2, 30%) were obtained from Xilong Chemical Co., Ltd. (Guangzhou, China). All reagents were used as received without further purification.

3.2. Preparation of Catalysts

Ni/Fe-MOF samples were synthesized using a solvothermal router similar to MIL-53(Fe), according to the previous literature [39]. In a typical synthesis, 9 mmol of H_2BDC, 6 mmol of $FeCl_3 \cdot 6H_2O$, and a certain amount of $Ni(NO_3)_2 \cdot 6H_2O$ were dissolved in 60 mL DMF. The obtained mixture was vigorously stirred for 30 min before being transferred into a 100 mL hydrothermal synthesis autoclave reactor 304 stainless steel high-pressure digestion tank with PTFE lining (Baoshishan Co., Ltd., Shanghai, China). The autoclave was heated at 100 °C in an oven (Memmert UN110, Schwabach, Germany) with a heating rate of 5 °C/min for three days. After being cooled to room temperature in air, the remaining H_2BDC was removed using a distillation method with DMF solvent for 24 h at 100 °C with a heating rate of 5 °C/min. The obtained suspension was centrifuged at 6000 rpm for 30 min, and the orange precipitates located at the bottom of the tube were washed with DMF (three times) and water (three times), respectively. Finally, the product was dried for 24 h at 60 °C. The obtained MOFs samples with corresponding Ni concentration were denoted as Ni/Fe-MOF-x (x is the molar ratio of Ni^{2+}/Fe^{3+}, and was chosen as 0, 0.1, 0.3, 0.5, and 0.7). The specific description is shown in Table S1 and the flow chart of the synthesis method is described in Figure S4. The sample was washed with DMF and water to obtain Ni/Fe-MOF-x·DMF and Ni/Fe-MOF-x·H_2O, respectively. For comparison, MIL(53) also was prepared using a similar method above without the presence of $Ni(NO_3)_2 \cdot 6H_2O$ in the reaction solution mixture.

3.3. Catalyst Characterization

Powder X-ray diffraction (XRD) patterns were conducted on a D8 Advance Bruker powder diffractometer with a Cu Kα source (λ = 0.15405) at a scan rate of 0.04°/s with 2θ = 2 to 30°. The surface morphologies and particle size of Ni/Fe-MOF samples were observed using field emission scanning electron microscope (FESEM, JEOL JSM-7600F, Peabody, MA, USA) equipped with an energy dispersive X-ray spectroscope (EDS, Oxford instruments 50 mm^2 X-Max, Abingdon, UK). FT-IR spectra were recorded on an EQUINOX 55 spectrometer (Bruker, Germany) using the KBr pellet technique. Raman spectroscopy was carried out on the HORIBA Jobin Yvon spectrometer with a laser beam of 633 nm. To examine the existence of Ni and Fe in the samples, X-ray photoelectron spectra (XPS) of the samples was measured using MultiLab 2000 spectrometer (Thermo VG Scientific, Waltham, MA, USA). The optical absorption characteristics of the photocatalysts were determined using ultraviolet-visible (UV/Vis) diffuse reflectance spectroscopy (UV/Vis DRS, Shimazu UV-2450, Kyoto, Japan) in the range 200–900 cm^{-1}. PL spectroscopy was performed using a Hitachi F4500 Fluorescence Spectrometer (Schaumburg, IL, USA) with the Xe Lamp Power range (700–900 V) at room temperature. The specific surface area and pore distribution of MIL-53(Fe) and Ni/Fe-MOFs

were determined using the Brunauer–Emmett–Teller (BET) method and Barrett–Joyner–Halenda (BJH) method, respectively (TriStar 3000 V6.07, Micromeritics instrument corporation, Norcross, GA, USA). The samples were kept at 200 °C for 5 h to degas. The pH value was measured using a pH meter (Consort-C1010, Turnhout, Belgium) at room temperature.

3.4. Photocatalytic Test

The photocatalytic activities of Ni/Fe-MOF photocatalysts were evaluated using the photodegradation of RhB under visible light irradiation with a 40 W compact fluorescent lamp (Philips) in the open air and at room temperature (Figure S5). The intensity and wavelength of the light source was 4400 lm and >400 nm, respectively (Figure S6 and Table S2). Therefore, it was suggested that the photocatalytic processes in our experiments were mainly due to the action of the visible light range [70–72]. In each run, a mixture of RhB aqueous solution (3.10^{-5} mol/L, 100 mL), the given catalyst (20 mg), and H_2O_2 (10^{-5} mol/L) was magnetically stirred in the presence or absence of light. Five milliliters of the suspension was withdrawn at the same intervals and immediately centrifuged to separate the photocatalyst particles for 15 min. The concentration of RhB was analyzed using a UV-visible spectrophotometer (Model Evolution 60S, Thermo Fisher Scientific, Waltham, MA, USA) at a maximum absorbance wavelength of λ = 554 nm. In addition, the effect of parameters including initial dye concentration and initial solution pH on the photodegradation of RhB over Ni/Fe-MOF photocatalysts was also investigated. pH levels of 3, 5, 7, and 9 were selected, whereas the concentrations of RhB were increased from 1.10^{-5} M to 4.10^{-5} M.

4. Conclusions

In summary, we have successfully prepared mixed Ni/Fe-base MOF with different molar ratios of Ni^{2+}/Fe^{3+} via a direct solvothermal approach. The structure characterization results from XRD, Raman, XPS, and FT-IR confirmed that with the presence of mixed ionic Fe^{3+} and Ni^{2+}, MIL-88B crystals based on the mixed metal Fe_2NiO cluster was formed, while MIL-53 (Fe) was formed with the presence of a single ion Fe^{3+}. The photocatalytic performance of the obtained photocatalysts was evaluated in the decolorization of RhB dye. The results indicated that the obtained Ni/Fe-MOF samples exhibited high photocatalytic activity in comparison to MIL-53(Fe). The degradation rate of Ni/Fe-MOF-0.3 could reach the highest (91.14%) after 180 min of visible light irradiation. These results suggest that the Ni/Fe-MOF, which consist mixed-metal cluster Fe_2NiO with electron transfer effects, might enhance the photocatalytic performance.

Conflicts of Interest: The authors declare no conflict of interest.

References

1. Tranchemontagne, D.J.; Mendoza-Cortés, J.L.; O'Keeffe, M.; Yaghi, O.M. Secondary building units, nets and bonding in the chemistry of metal-organic frameworks. *Chem. Soc. Rev.* **2009**, *38*, 1257–1283. [CrossRef] [PubMed]

2. Hamon, L.; Serre, C.; Devic, T.; Loiseau, T.; Millange, F.; Férey, G.; De Weireld, G. Comparative study of hydrogen sulfide adsorption in the MIL-53(Al, Cr, Fe), MIL-47(V), MIL-100(Cr), and MIL-101(Cr) metal-organic frameworks at room temperature. *J. Am. Chem. Soc.* **2009**, *131*, 8775–8777. [CrossRef] [PubMed]

3. Devic, T.; Salles, F.; Bourrelly, S.; Moulin, B.; Maurin, G.; Horcajada, P.; Serre, C.; Vimont, A.; Lavalley, J.C.; Leclerc, H.; et al. Effect of the organic functionalization of flexible MOFs on the adsorption of CO_2. *J. Mater. Chem.* **2012**, *22*, 10266–10273. [CrossRef]

4. Vu, T.A.; Le, G.H.; Dao, C.D.; Dang, L.Q.; Nguyen, K.T.; Nguyen, Q.K.; Dang, P.T.; Tran, H.T.K.; Duong, Q.T.; Nguyen, T.V.; et al. Arsenic removal from aqueous solutions by adsorption using novel MIL-53(Fe) as a highly efficient adsorbent. *RSC Adv.* **2015**, *5*, 5261–5268. [CrossRef]

5. Jia, J.; Xu, F.; Long, Z.; Hou, X.; Sepaniak, M.J. Metal–organic framework MIL-53(Fe) for highly selective and ultrasensitive direct sensing of MeHg+. *Chem. Commun.* **2013**, *49*, 4670. [CrossRef] [PubMed]

6. Gao, X.; Zhai, M.; Guan, W.; Liu, J.; Liu, Z.; Damirin, A. Controllable synthesis of a smart multifunctional nanoscale metal-organic framework for magnetic resonance/optical imaging and targeted drug delivery. *ACS Appl. Mater. Interfaces* **2017**, *9*, 3455–3462. [CrossRef] [PubMed]

7. Bach, L.G.; Van Tran, T.; Nguyen, T.D.; Van Pham, T.; Do, S.T. Enhanced adsorption of methylene blue onto graphene oxide-doped XFe_2O_4(X = Co, Mn, Ni) nanocomposites: Kinetic, isothermal, thermodynamic and recyclability studies. *Res. Chem. Intermed.* **2018**, *44*, 1661–1687. [CrossRef]

8. Nhung, N.T.H.; Quynh, B.T.P.; Thao, P.T.T.; Bich, H.N.; Giang, B.L. Pretreated Fruit Peels as Adsorbents for Removal of Dyes from Water. *IOP Conf. Ser. Earth Environ. Sci.* **2018**, *159*, 012015. [CrossRef]

9. Kim, D.W.; Bach, L.G.; Hong, S.S.; Park, C.; Lim, K.T. A Facile Route towards the Synthesis of Fe_3O_4/Graphene Oxide Nanocomposites for Environmental Applications. *Mol. Cryst. Liq. Cryst.* **2014**. [CrossRef]

10. Van Thuan, T.; Ho, V.T.T.; Trinh, N.D.; Thuong, N.T.; Quynh, B.T.P.; Bach, L.G. Facile one-spot synthesis of highly porous KOH-activated carbon from rice husk: Response surface methodology approach. *Carbon Sci. Technol.* **2016**, *8*, 63–69.

11. Trinh, N.D.; Hong, S.-S. Photocatalytic Decomposition of Methylene Blue Over MIL-53 (Fe) Prepared Using Microwave-Assisted Process Under Visible Light Irradiation. *J. Nanosci. Nanotechnol.* **2015**, *15*, 5450–5454. [CrossRef] [PubMed]

12. Yang, S.J.; Im, J.H.; Kim, T.; Lee, K.; Park, C.R. MOF-derived ZnO and ZnO@C composites with high photocatalytic activity and adsorption capacity. *J. Hazard. Mater.* **2011**, *186*, 376–382. [CrossRef] [PubMed]

13. Du, J.J.; Yuan, Y.P.; Sun, J.X.; Peng, F.M.; Jiang, X.; Qiu, L.G.; Xie, A.J.; Shen, Y.H.; Zhu, J.F. New photocatalysts based on MIL-53 metal-organic frameworks for the decolorization of methylene blue dye. *J. Hazard. Mater.* **2011**, *190*, 945–951. [CrossRef] [PubMed]

14. Zhang, C.; Ai, L.; Jiang, J. Solvothermal synthesis of MIL-53(Fe) hybrid magnetic composites for photoelectrochemical water oxidation and organic pollutant photodegradation under visible light. *J. Mater. Chem. A* **2015**, *3*, 3074–3081. [CrossRef]

15. Alhamami, M.; Doan, H.; Cheng, C.H. A review on breathing behaviors of metal-organic-frameworks (MOFs) for gas adsorption. *Materials* **2014**, *7*, 3198–3250. [CrossRef] [PubMed]

16. Dhakshinamoorthy, A.; Alvaro, M.; Garcia, H. Commercial metal-organic frameworks as heterogeneous catalysts. *Chem. Commun.* **2012**, *48*, 11275–11288. [CrossRef] [PubMed]

17. Ai, L.; Zhang, C.; Li, L.; Jiang, J. Iron terephthalate metal-organic framework: Revealing the effective activation of hydrogen peroxide for the degradation of organic dye under visible light irradiation. *Appl. Catal. B Environ.* **2014**, *148–149*, 191–200. [CrossRef]

18. Lionet, Z.; Kamata, Y.; Nishijima, S.; Toyao, T.; Kim, T.-H.; Horiuchi, Y.; Lee, S.W.; Matsuoka, M. Water oxidation reaction promoted by MIL-101(Fe) photoanode under visible light irradiation. *Res. Chem. Intermed.* **2018**, *44*, 4755–4764. [CrossRef]

19. Qu, L.-L.; Wang, J.; Xu, T.-Y.; Chen, Q.-Y.; Chen, J.-H.; Shi, C.-J. Iron(iii)-based metal–organic frameworks as oxygen-evolving photocatalysts for water oxidation. *Sustain. Energy Fuels* **2018**, *2*, 2109–2114. [CrossRef]

20. Wang, D.; Li, Z. Iron-based metal–organic frameworks (MOFs) for visible-light-induced photocatalysis. *Res. Chem. Intermed.* **2017**, *43*, 5169–5186. [CrossRef]

21. Wang, D.; Albero, J.; García, H.; Li, Z. Visible-light-induced tandem reaction of o-aminothiophenols and alcohols to benzothiazoles over Fe-based MOFs: Influence of the structure elucidated by transient absorption spectroscopy. *J. Catal.* **2017**, *349*, 156–162. [CrossRef]

22. Horiuchi, Y.; Toyao, T.; Miyahara, K.; Zakary, L.; Do Van, D.; Kamata, Y.; Kim, T.-H.; Lee, S.W.; Matsuoka, M. Visible-light-driven photocatalytic water oxidation catalysed by iron-based metal–organic frameworks. *Chem. Commun.* **2016**, *52*, 5190–5193. [CrossRef] [PubMed]

23. Hu, L.; Deng, G.; Lu, W.; Pang, S.; Hu, X. Deposition of CdS nanoparticles on MIL-53(Fe) metal-organic framework with enhanced photocatalytic degradation of RhB under visible light irradiation. *Appl. Surf. Sci.* **2017**, *410*, 401–413. [CrossRef]

24. Zhou, Y.; Mao, Z.; Wang, W.; Yang, Z.; Liu, X. In-Situ Fabrication of Graphene Oxide Hybrid Ni-Based Metal-Organic Framework (Ni-MOFs@GO) with Ultrahigh Capacitance as Electrochemical Pseudocapacitor Materials. *ACS Appl. Mater. Interfaces* **2016**, *8*, 28904–28916. [CrossRef] [PubMed]

25. Panda, R.; Rahut, S.; Basu, J.K. Preparation of a Fe_2O_3/MIL-53(Fe) composite by partial thermal decomposition of MIL-53(Fe) nanorods and their photocatalytic activity. *RSC Adv.* **2016**, *6*, 80981–80985. [CrossRef]

26. Lou, X.; Hu, H.; Li, C.; Hu, X.; Li, T.; Shen, M.; Chen, Q.; Hu, B. Capacity control of ferric coordination polymers by zinc nitrate for lithium-ion batteries. *RSC Adv.* **2016**, *6*, 86126–86130. [CrossRef]

27. Vuong, G.T.; Pham, M.H.; Do, T.O. Synthesis and engineering porosity of a mixed metal Fe2Ni MIL-88B metal-organic framework. *Dalt. Trans.* **2013**, *42*, 550–557. [CrossRef] [PubMed]

28. Vuong, G.-T.; Pham, M.-H.; Do, T.-O. Direct synthesis and mechanism of the formation of mixed metal Fe2Ni-MIL-88B. *CrystEngComm* **2013**, *15*, 9694. [CrossRef]

29. Pham, M.-H.; Dinh, C.-T.; Vuong, G.-T.; Ta, N.-D.; Do, T.-O. Visible light induced hydrogen generation using a hollow photocatalyst with two cocatalysts separated on two surface sides. *Phys. Chem. Chem. Phys.* **2014**, *16*, 5937. [CrossRef] [PubMed]

30. Sun, Q.; Liu, M.; Li, K.; Han, Y.; Zuo, Y.; Chai, F.; Song, C.; Zhang, G.; Guo, X. Synthesis of Fe/M (M = Mn, Co, Ni) bimetallic metal organic frameworks and their catalytic activity for phenol degradation under mild conditions. *Inorg. Chem. Front.* **2017**, *4*, 144–153. [CrossRef]

31. Díaz-Gallifa, P.; Fabelo, O.; Pasán, J.; Cañadillas-Delgado, L.; Lloret, F.; Julve, M.; Ruiz-Pérez, C. Two-dimensional 3d-4f heterometallic coordination polymers: Syntheses, crystal structures, and magnetic properties of six new Co(II)-Ln(III) compounds. *Inorg. Chem.* **2014**, *53*, 6299–6308. [CrossRef] [PubMed]

32. Vu, T.A.; Le, G.H.; Dao, C.D.; Dang, L.Q.; Nguyen, K.T.; Dang, P.T.; Tran, H.T.K.; Duong, Q.T.; Nguyen, T.V.; Lee, G.D. Isomorphous substitution of Cr by Fe in MIL-101 framework and its application as a novel heterogeneous photo-Fenton catalyst for reactive dye degradation. *RSC Adv.* **2014**, *40*, 41185–41194. [CrossRef]

33. Zhu, W.; Liu, P.; Xiao, S.; Wang, W.; Zhang, D.; Li, H. Microwave-assisted synthesis of Ag-doped MOFs-like organotitanium polymer with high activity in visible-light driven photocatalytic NO oxidization. *Appl. Catal. B Environ.* **2015**, *172–173*, 46–51. [CrossRef]

34. Han, Y.; Liu, M.; Li, K.; Sun, Q.; Zhang, W.; Song, C.; Zhang, G.; Conrad Zhang, Z.; Guo, X. In situ synthesis of titanium doped hybrid metal-organic framework UiO-66 with enhanced adsorption capacity for organic dyes. *Inorg. Chem. Front.* **2017**, *4*, 1870–1880. [CrossRef]

35. Vinh, N.H.; Long Giang, B.; Sy Trung, D.; Thuong, N.T.; Trinh, N.D. Photoluminescence Properties of Eu-Doped MIL-53(Fe) Obtained by Solvothermal Synthesis. *J. Nanosci. Nanotechnol.* **2019**, *19*, 1148–1150.

36. Chi, Y.X.; Niu, S.Y.; Jin, J. Syntheses, structures and photophysical properties of a series of Zn-Ln coordination polymers (Ln = Nd, Pr, Sm, Eu, Tb, Dy). *Inorg. Chim. Acta* **2009**, *362*, 3821–3828. [CrossRef]

37. Tahir, M. Synergistic effect in MMT-dispersed Au/TiO2 monolithic nanocatalyst for plasmon-absorption and metallic interband transitions dynamic CO_2 photo-reduction to CO. *Appl. Catal. B Environ.* **2017**, *219*, 329–343. [CrossRef]

38. Tahir, M. Ni/MMT-promoted TiO2 nanocatalyst for dynamic photocatalytic H_2 and hydrocarbons production from ethanol-water mixture under UV-light. *Int. J. Hydrogen Energy* **2017**, *42*, 28309–28326. [CrossRef]

39. Haque, E.; Khan, N.; Park, H.J.; Jhung, S.H. Synthesis of a metal-organic framework material, iron terephthalate, by ultrasound, microwave, and conventional electric heating: A kinetic study. *Chem. A Eur. J.* **2010**, *16*, 1046–1052. [CrossRef] [PubMed]

40. Pu, M.; Guan, Z.; Ma, Y.; Wan, J.; Wang, Y.; Brusseau, M.L.; Chi, H. Synthesis of iron-based metal-organic framework MIL-53 as an efficient catalyst to activate persulfate for the degradation of Orange G in aqueous solution. *Appl. Catal. A Gen.* **2018**, *549*, 82–92. [CrossRef] [PubMed]

41. Feng, X.; Chen, H.; Jiang, F. In-situ ethylenediamine-assisted synthesis of a magnetic iron-based metal-organic framework MIL-53(Fe) for visible light photocatalysis. *J. Colloid Interface Sci.* **2017**, *494*, 32–37. [CrossRef] [PubMed]

42. Shannon, R.D. Revised effective ionic radii and systematic studies of interatomic distances in halides and chalcogenides. *Acta Crystallogr. Sect. A* **1976**, *32*, 751–767. [CrossRef]

43. Nakamoto, K. Applications in Organometallic Chemistry. In *Infrared and Raman Spectra of Inorganic and Coordination Compounds*; John Wiley & Sons, Inc.: Hoboken, NJ, USA; pp. 275–331, ISBN 9780470405888.

44. Gao, Y.; Li, S.; Li, Y.; Yao, L.; Zhang, H. Accelerated photocatalytic degradation of organic pollutant over metal-organic framework MIL-53(Fe) under visible LED light mediated by persulfate. *Appl. Catal. B Environ.* **2017**, *202*, 165–174. [CrossRef]

45. Vu, T.A.; Le, G.H.; Vu, H.T.; Nguyen, K.T.; Quan, T.T.T.; Nguyen, Q.K.; Tran, H.T.K.; Dang, P.T.; Vu, L.D.; Lee, G.D. Highly photocatalytic activity of novel Fe-MIL-88B/GO nanocomposite in the degradation of reactive dye from aqueous solution. *Mater. Res. Express* **2017**, *4*, 035038. [CrossRef]

46. Islam, M.R.; Bach, L.G.; Vo, T.S.; Tran, T.N.; Lim, K.T. Nondestructive chemical functionalization of MWNTs by poly(2-dimethylaminoethyl methacrylate) and their conjugation with CdSe quantum dots: Synthesis, properties, and cytotoxicity studies. *Appl. Surf. Sci.* **2013**. [CrossRef]

47. Grosvenor, A.P.; Kobe, B.A.; Biesinger, M.C.; McIntyre, N.S. Investigation of multiplet splitting of Fe 2p XPS spectra and bonding in iron compounds. *Surf. Interface Anal.* **2004**, *36*, 1564–1574. [CrossRef]

48. Molchan, I.S.; Thompson, G.E.; Skeldon, P.; Lindsay, R.; Walton, J.; Kouvelos, E.; Romanos, G.E.; Falaras, P.; Kontos, A.G.; Arfanis, M.; et al. Microscopic study of the corrosion behaviour of mild steel in ionic liquids for CO_2 capture applications. *RSC Adv.* **2015**, *5*, 35181–35194. [CrossRef]

49. Lian, K.K.; Kirk, D.W.; Thorpe, S.J. Investigation of a "Two-State" Tafel Phenomenon for the Oxygen Evolution Reaction on an Amorphous Ni-Co Alloy. *J. Electrochem. Soc.* **1995**, *142*, 3704–3712. [CrossRef]

50. Siang, T.J.; Bach, L.G.; Singh, S.; Truong, Q.D.; Ho, V.T.T.; Huy Phuc, N.H.; Alenazey, F.; Vo, D.V.N. Methane bi-reforming over boron-doped Ni/SBA-15 catalyst: Longevity evaluation. *Int. J. Hydrogen Energy* **2018**. [CrossRef]

51. Sing, K.S.W. Reporting physisorption data for gas/solid systems with special reference to the determination of surface area and porosity (Recommendations 1984). *Pure Appl. Chem.* **1985**, *57*, 603–619. [CrossRef]

52. Horcajada, P.; Serre, C.; Maurin, G.; Ramsahye, N.A.; Balas, F.; Vallet-Regí, M.; Sebban, M.; Taulelle, F.; Férey, G. Flexible porous metal-organic frameworks for a controlled drug delivery. *J. Am. Chem. Soc.* **2008**, *130*, 6774–6780. [CrossRef] [PubMed]

53. Blake, A.B.; Yavari, A.; Hatfield, W.E.; Sethulekshmi, C.N. Magnetic and spectroscopic properties of some heterotrinuclear basic acetates of chromium(III), iron(III), and divalent metal ions. *J. Chem. Soc. Dalt. Trans.* **1985**, 2509–2520. [CrossRef]

54. Zhang, Z.; Li, X.; Liu, B.; Zhao, Q.; Chen, G. Hexagonal microspindle of NH2-MIL-101(Fe) metal-organic frameworks with visible-light-induced photocatalytic activity for the degradation of toluene. *RSC Adv.* **2016**, *6*, 4289–4295. [CrossRef]

55. Nguyen, M.T.H.; Nguyen, Q.T. Efficient refinement of a metal-organic framework MIL-53(Fe) by UV-vis irradiation in aqueous hydrogen peroxide solution. *J. Photochem. Photobiol. A Chem.* **2014**, *288*, 55–59. [CrossRef]

56. Ling, S.; Slater, B. Unusually Large Band Gap Changes in Breathing Metal-Organic Framework Materials. *J. Phys. Chem. C* **2015**, *119*, 16667–16677. [CrossRef]

57. Hou, Y.; Yuan, H.; Chen, H.; Feng, J.; Ding, Y.; Li, L. Preparation of La^{3+}/Zn^{2+}-doped BiVO4 nanoparticles and its enhanced visible photocatalytic activity. *Appl. Phys. A* **2017**, *123*, 611. [CrossRef]

58. Dutta, D.P.; Ballal, A.; Chopade, S.; Kumar, A. A study on the effect of transition metal (Ti^{4+}, Mn^{2+}, Cu^{2+} and Zn^{2+})-doping on visible light photocatalytic activity of Bi_2MoO_6 nanorods. *J. Photochem. Photobiol. A Chem.* **2017**, *346*, 105–112. [CrossRef]

59. Jin, A.Z.; Dong, W.; Yang, M.; Wang, J.; Wang, G.; Jin, Z.; Dong, W.; Yang, M.; Wang, J.; Wang, G. One-pot Preparation of Hierarchical Nanosheet-Constructed Fe_3O_4/MIL-88B (Fe) Magnetic Microspheres with High Efficiency Photocatalytic Degradation of Dye. *ChemCatChem* **2016**, *22*, 3510–3517. [CrossRef]

60. Liang, R.; Luo, S.; Jing, F.; Shen, L.; Qin, N.; Wu, L. A simple strategy for fabrication of Pd@MIL-100(Fe) nanocomposite as a visible-light-driven photocatalyst for the treatment of pharmaceuticals and personal care products (PPCPs). *Appl. Catal. B Environ.* **2015**, *176–177*, 240–248. [CrossRef]

61. Laurier, K.G.M.; Vermoortele, F.; Ameloot, R.; De Vos, D.E.; Hofkens, J.; Roeffaers, M.B.J. Iron(III)-based metal-organic frameworks as visible light photocatalysts. *J. Am. Chem. Soc.* **2013**, *135*, 14488–14491. [CrossRef] [PubMed]

62. Martínez, F.; Leo, P.; Orcajo, G.; Díaz-García, M.; Sanchez-Sanchez, M.; Calleja, G. Sustainable Fe-BTC catalyst for efficient removal of mehylene blue by advanced fenton oxidation. *Catal. Today* **2018**, *313*, 6–11. [CrossRef]

63. Gao, C.; Chen, S.; Quan, X.; Yu, H.; Zhang, Y. Enhanced Fenton-like catalysis by iron-based metal organic frameworks for degradation of organic pollutants. *J. Catal.* **2017**, *356*, 125–132. [CrossRef]

64. Liu, Q.; Liu, Y.; Gao, B.; Chen, Y.; Lin, B. Hydrothermal synthesis of In_2O_3-loaded BiVO4 with exposed {010}{110} facets for enhanced visible-light photocatalytic activity. *Mater. Res. Bull.* **2017**, *87*, 114–118. [CrossRef]

65. Sotnik, S.A.; Polunin, R.A.; Kiskin, M.A.; Kirillov, A.M.; Dorofeeva, V.N.; Gavrilenko, K.S.; Eremenko, I.L.; Novotortsev, V.M.; Kolotilov, S.V. Heterometallic coordination polymers assembled from trigonal trinuclear Fe_2Ni-pivalate blocks and polypyridine spacers: Topological diversity, sorption, and catalytic properties. *Inorg. Chem.* **2015**, *54*, 5169–5181. [CrossRef] [PubMed]

66. Jiang, Q.; Håkansson, M.; Suomi, J.; Ala-Kleme, T.; Kulmala, S. Cathodic electrochemiluminescence of lucigenin at disposable oxide-coated aluminum electrodes. *J. Electroanal. Chem.* **2006**, *591*, 85–92. [CrossRef]

67. Van Thuan, T.; Quynh, B.T.P.; Nguyen, T.D.; Ho, V.T.T.; Bach, L.G. Response surface methodology approach for optimization of Cu^{2+}, Ni^{2+} and Pb^{2+} adsorption using KOH-activated carbon from banana peel. *Surf. Interfaces* **2017**, *6*, 209–217. [CrossRef]

68. Van Tran, T.; Bui, Q.T.P.; Nguyen, T.D.; Le, N.T.H.; Bach, L.G. A comparative study on the removal efficiency of metal ions (Cu^{2+}, Ni^{2+}, and Pb^{2+}) using sugarcane bagasse-derived ZnCl2-activated carbon by the response surface methodology. *Adsorpt. Sci. Technol.* **2017**, *35*, 72–85. [CrossRef]

69. Van Tran, T.; Bui, Q.T.P.; Nguyen, T.D.; Thanh Ho, V.T.; Bach, L.G. Application of response surface methodology to optimize the fabrication of $ZnCl_2$-activated carbon from sugarcane bagasse for the removal of Cu^{2+}. *Water Sci. Technol.* **2017**, *75*, 2047–2055. [CrossRef] [PubMed]

70. Dinh, C.-T.; Nguyen, T.-D.; Kleitz, F.; Do, T.-O. Large-scale synthesis of uniform silver orthophosphate colloidal nanocrystals exhibiting high visible light photocatalytic activity. *Chem. Commun.* **2011**, *47*, 7797–7799. [CrossRef] [PubMed]

71. Yu, X.; Cohen, S.M. Photocatalytic metal-organic frameworks for the aerobic oxidation of arylboronic acids. *Chem. Commun.* **2015**, *51*, 9880–9883. [CrossRef] [PubMed]

72. Lam, S.M.; Sin, J.C.; Abdullah, A.Z.; Mohamed, A.R. Efficient photodegradation of resorcinol with Ag_2O/ZnO nanorods heterostructure under a compact fluorescent lamp irradiation. *Chem. Pap.* **2013**, *67*, 1277–1284. [CrossRef]